J. Fluid Mech. (2003), *vol.* 493, *pp.* 277–286.
DOI: 10.1017/S0022112003005822 Printed in the United Kingdom

Vortex-induced instability of an incompressible wall-bounded shear layer

By T. K. SENGUPTA[1], S. DE[2] AND S. SARKAR[2]

[1]Department of Aerospace Engineering, IIT Kanpur 208 016, India
[2]Department of Mechanical Engineering, IIT Kanpur 208 016, India

(Received 7 April 2003 and in revised form 1 July 2003)

The unsteady separated flow produced by a finite-core vortex on a plane shear layer is studied here as a vortex-induced instability. The mechanism of such an interaction, where the distance between the wall and the vortex is many times the local boundary layer thickness, is shown here by flow visualization and the solution of the unsteady Navier–Stokes equation. A new theory is proposed here, which is generic to the Navier–Stokes equation without any assumptions, that is based on growth of disturbance energy in time. A dynamical systems approach based on the proper orthogonal decomposition technique is used to provide a quantitative measure.

1. Introduction

The interaction between a convecting finite-core vortex and an underlying shear layer is important, as it typifies (*a*) unsteady flow separation processes (as discussed in Degani, Walker & Smith 1998; Obabko & Cassel 2002 and references therein) and (*b*) flow transition that bypasses the usual linear instability route (Brinckman & Walker 2001). The idea that a distant vortex can induce a small longitudinal adverse pressure gradient which destabilizes a wall-bounded flow was postulated first by Taylor (1936) while studying the dependence of critical Reynolds number upon free-stream turbulence (FST). Monin & Yaglom (1971) in discussing this work noted that the change in critical Reynolds number by the small longitudinal adverse pressure gradient is due to a sequence of unsteady separation, presumably created by a train of vortices embedded in the FST. The assumption implicit in this scenario is that the effect is connected with the generation of fluctuations of longitudinal pressure gradient by these disturbances, leading to the random formation of individual spots of unstable *S*-shaped velocity profiles (Monin & Yaglom 1971).

The interaction of a shear layer with a finite-core vortex leading to unsteady separation was noted by Doligalski, Smith & Walker (1994) as one of the most important unsolved problems of fluid dynamics. Such unsteady separation is present in (i) flow past surface-mounted obstacles; (ii) dynamic stall and blade vortex interaction; (iii) impulsive motion of bluff bodies; (iv) bypass transition and (v) near-wall turbulence.

The instability mechanism that we provide here by a simplified model experiment and theory based on the Navier–Stokes equation should also be relevant to the generation of hairpins in near-wall turbulence (see Smith *et al.* 1991 and Robinson 1991), which are three-dimensional and more complicated. In Sengupta, Lim & Chattopadhyay (2001) a vortex with finite core size was created experimentally by a rotating and translating a circular cylinder whose strength (Γ), distance from the

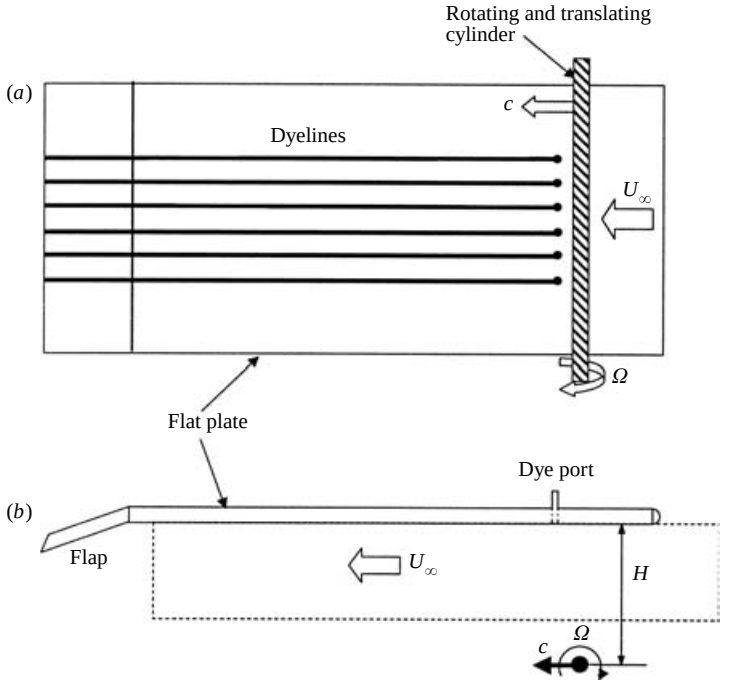

FIGURE 1. Schematic of the experimental set-up. (*a*) Side view and (*b*) top view as seen in the tunnel. Broken line boundary in (*b*) indicates the computational domain.

plate (H) and the circulation sign were controlled accurately. The main emphasis of the experiment was to control all the relevant parameters so that any observed events can be reproduced. In figure 1 the schematic of the flow is shown. It was seen that a slowly convecting vortex, of anticlockwise circulation, creates transition/unsteady separation ahead of it. The theoretical explanation was based upon the time evolution of the disturbance energy (E_d), which is governed by

$$\nabla^2 E_d = 2\boldsymbol{\omega}_m \cdot \boldsymbol{\omega}_d + \boldsymbol{\omega}_d \cdot \boldsymbol{\omega}_d - \boldsymbol{V}_m \cdot \nabla \times \boldsymbol{\omega}_d - \boldsymbol{V}_d \cdot \nabla \times \boldsymbol{\omega}_m - \boldsymbol{V}_d \cdot \nabla \times \boldsymbol{\omega}_d. \qquad (1.1)$$

In this equation $\boldsymbol{V}$ and $\boldsymbol{\omega}$ represent velocity and vorticity fields respectively. The subscripts m and d refer to mean and disturbance quantities. Disturbance energy grows when the right-hand side of (1.1) becomes negative. This generic mechanism is based on the full Navier–Stokes equation without any simplifying assumptions. The receptivity aspect of the problem was established in Sengupta *et al.* (2001); here a detailed computation that includes the leading edge of the plate is reported.

2. An experimental observation of vortex-induced instability

The experiment described in Sengupta *et al.* (2001) was performed in a recirculating water tunnel. One of their cases is reproduced here to highlight a receptivity mechanism of a shear layer to a convecting vortex in the free stream. In this experiment the boundary layer was formed on a flat plate, held vertically on its edge in the tunnel. A coherent bound vortex is created by rotating a circular cylinder of diameter 15 mm, whose axis was along the spanwise direction of the plate. The cylinder can be rotated in either direction and was rotated at $\Omega = 5$ r.p.s. in the anticlockwise direction, for

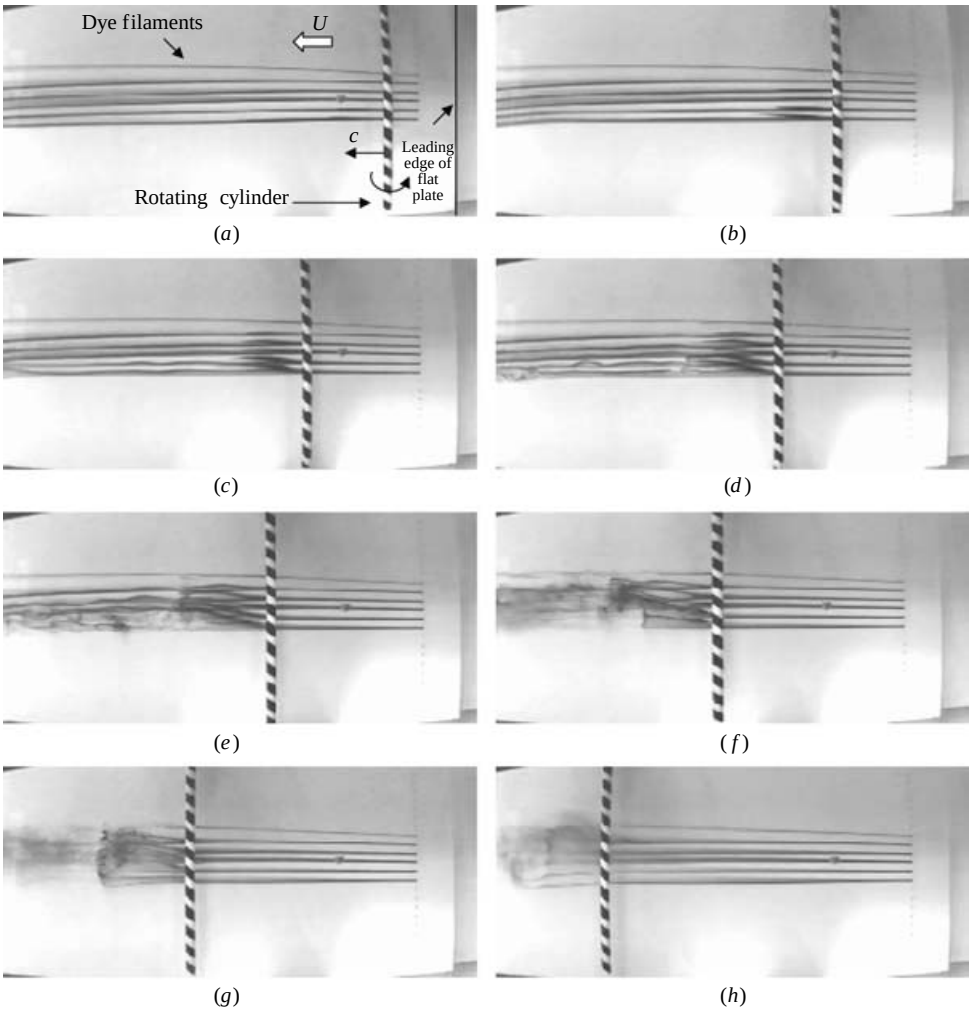

FIGURE 2. Bypass transition created by a counter-rotating vortex for $U_\infty = 16.26\,\mathrm{cm\,s^{-1}}$, $c = 0.154$, $H = 9\,\mathrm{cm}$ and $\Omega = +5$ r.p.s.

the case shown in figure 2. For flow visualization, food dye was released from six dye ports located 88 mm downstream from the leading edge of the plate.

The Reynolds number based on the diameter of the cylinder and free stream speed ($U_\infty = 162\,\mathrm{mm\,s^{-1}}$) was 2600. The cylinder was convected at $c = 0.15U_\infty$, at a height $H = 90\,\mathrm{mm}$. The ratio of surface speed to the relative speed of the free stream and cylinder was 1.71. The noise level of the water channel is 1% at maximum speed. It is known (Badr *et al.* 1990) that a rotating cylinder ceases to shed the coherent vortices associated with Kármán vortex streets when the surface speed is more than 1.5 times the free-stream speed. In this experiment the bound vortex circulation is fixed by controlling the rotation rate of the cylinder and this controls the dynamics of the flow.

In figure 2 flow visualization sequences indicate unsteady separation followed by bypass transition in frames (*b–h*). The dye filaments are essentially parallel at the onset (as in frames *a–d*), showing overall two-dimensionality during this stage. In frame (*b*), the dye filaments released very close to the plate lifted up due to the imposed

disturbances, with negligible spanwise spreading. The location where unsteadiness is seen is laminar in the absence of the convecting vortex, indicating the subcritical nature of the instabilities. Only flow visualization was used, as intrusive measurements changed the dynamics drastically. Therefore to quantify the experimental observation we have undertaken a numerical simulation of the problem described next. As we are interested in the onset stage of the instability, it is sufficient to perform a two-dimensional simulation of Navier–Stokes equation.

3. Numerical simulation of vortex-induced instability

In the present computations, the Navier–Stokes equation is solved in stream function–vorticity formulation, as in Brinckman & Walker (2001) and Obabko & Cassel (2002). Brinckman & Walker (2001) simulated the burst sequence of turbulent boundary layer excited by streamwise vortices (in the x-direction) for which a stream function is defined in the (y, z)-plane. Here the vorticity transport equation and the stream function equation are solved in (x, y)-plane,

$$\frac{\partial \boldsymbol{\omega}}{\partial t} + (\boldsymbol{V}\cdot\nabla)\boldsymbol{\omega} = \frac{1}{Re}\nabla^2\boldsymbol{\omega}, \tag{3.1}$$

$$\nabla^2\psi = -\boldsymbol{\omega}. \tag{3.2}$$

The non-dimensionalized equations have been obtained with the diameter of the cylinder as the length scale and the free-stream speed of the oncoming flow as the velocity scale. From these two scales the time scale is constructed and all the computational results are in non-dimensional units.

To solve (3.1) and (3.2) in the computational domain of figure 1(b) the parameters are as given in the previous section except for the strength of the convecting vortex which cannot be measured and is treated here as the parameter of the problem. For the present computation this is taken as $\Gamma = 9.1$. The Reynolds number based on displacement thickness of the undisturbed flow at the outflow is 472. Thus the flow is subcritical in the computational domain.

The domain is given by $-1 \leqslant x \leqslant 25$ with a uniformly spaced grid in the streamwise direction ($\Delta x = 0.04$) and $0 \leqslant y \leqslant 1.92$ with an arithmetically progressing grid in the wall normal direction with 141 points, and the wall resolution is given by $\Delta y_{wall} = 7.083 \times 10^{-4}$. In Brinckman & Walker (2001) and Obabko & Cassel (2002), the numerical methods used were $O(\Delta x \Delta t, \Delta y \Delta t)$ accurate. In contrast, the present computations use high-accuracy compact schemes for spatial discretization as described in Haras & Ta'asan (1994) and Sengupta, Anuradha & De (2003*a*), which has more than seven times higher spectral resolution than second-order-accurate schemes. The results reported here are grid independent, a coarser mesh having produced the same results.

At the inflow and the top-lid of the computational domain, one can calculate the stream function induced by Biot-Savart interaction due to the convecting vortex outside the computational domain. The wall boundary conditions correspond to no-slip. At the outflow the fully developed condition on the wall-normal component of velocity is used. The above conditions are used in equation (3.2) to derive the vorticity values at all boundary segments. The flow is started impulsively with the initial location of the vortex being $4D$ ahead of the leading edge.

In figure 3, identical stream function and vorticity contours are plotted at three times. As the free-stream vortex convects at a constant height its instantaneous streamwise location is shown by an arrowhead. At $t = 35$ there is a single separation bubble.

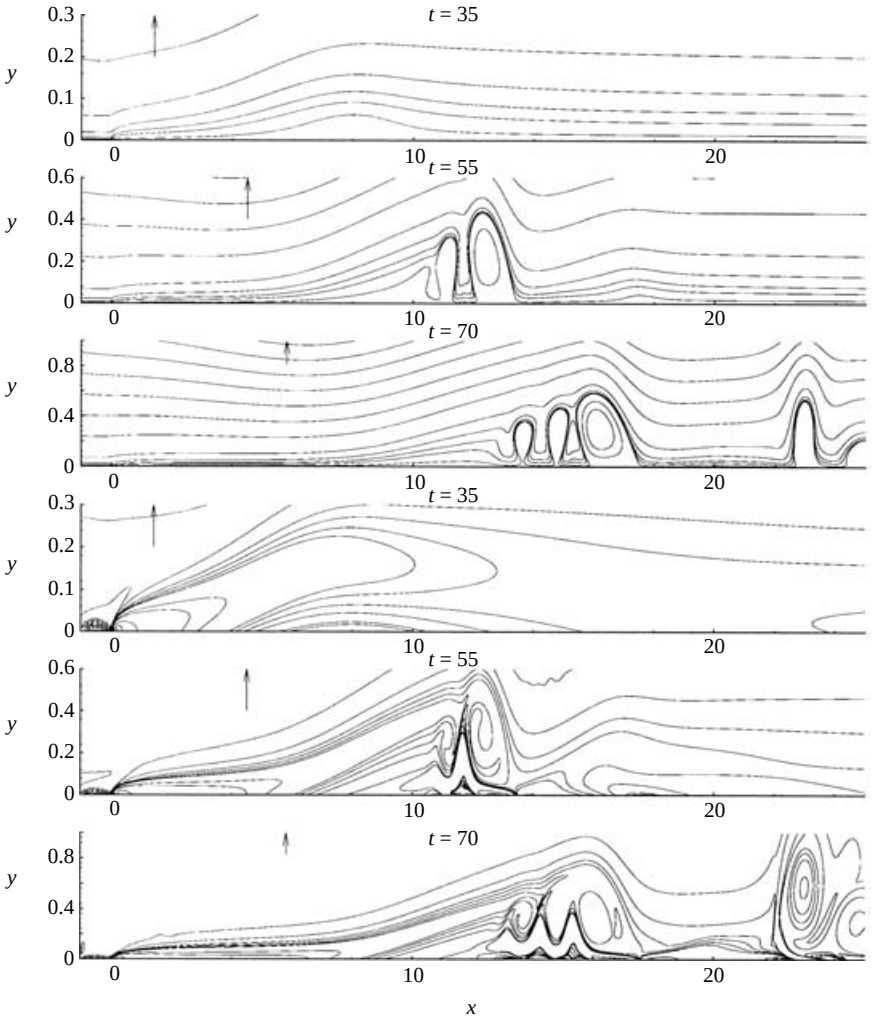

FIGURE 3. Stream function (top three panels) and vorticity contours at indicated times. Same contour values have been plotted for each quantity. Arrowheads at the top show the streamwise location of the convecting vortex.

By $t = 55$ this bubble suffers multiple interactions with vortices of opposite signs. These vortices also induce another vortex ahead of this cluster, clearly visible at $t = 70$. These bubbles on the wall were conjectured in Monin & Yaglom (1971) to be a result of buffeting of the shear layer by FST vortices. In the present study no modelling is required, all the effects are governed by the Navier–Stokes equation. For example, the primary vortex forms as a consequence of unsteady flow evolution and does not move at constant speed, unlike that modelled as a Batchelor vortex moving at constant speed in Obabko & Cassel (2002).

The unsteady separation and vortical structures near the wall are created due to the effects of the free-stream convecting vortex. A theoretical explanation of this is provided in Sengupta *et al.* (2002), where it is shown that shear layers can support disturbances created by sources inside or outside a shear layer by what is referred to as wall- and free-stream modes respectively. When free-stream modes are excited, as

seen here, they in turn cause the wall mode to be excited, by a coupling mechanism that ensures homogeneous boundary conditions at the wall.

The growth of the primary bubble and appearance of subsequent separation bubbles are due to an instability where the disturbance field is enriched from the primary flow. The conditions and mechanism by which these instabilities appear is discussed next.

4. The instability mechanism

The experimental and accompanying computational results display the existence of a receptivity mechanism inside the shear layer as a consequence of a single vortex migrating in the free stream at a constant speed. The role of various parameters responsible for this instability has been discussed in Sengupta *et al.* (2001). According to Landahl & Mollo-Christensen (1992) "the turbulent energy equation ... illustrate how Reynolds shear stress can do work against the mean velocity shear and transfer energy from the mean flow to the fluctuating field". To do this the authors emphasized that "it is possible to understand such behaviour by studying the redistribution of the total mechanical energy of the flow" [not just how the 'energy of perturbation' given by the square of the fluctuating velocity changes locally with time]. Hence an equation for total mechanical energy ($E = p/\rho + \frac{1}{2}V^2$) is first derived. For incompressible flows this is obtained by taking the divergence of the rotational form of the Navier–Stokes equation given by

$$\nabla^2 E = \boldsymbol{\omega}^2 - \boldsymbol{V} \cdot \nabla \times \boldsymbol{\omega}. \tag{4.1}$$

Thus the total mechanical energy is directly related to rotationality of the flow. It is not necessary to solve this equation to describe the flow instability, because in (4.1) the sign of the right-hand side indicates the presence of a source or a sink of E, is given by the property of the Poisson equation (Sommerfeld 1949). A negative sign signifies a local source. The vorticity field stabilizes E as shown in (4.1). However, the disturbance energy can grow via the vorticity product term of (1.1) when primary and disturbance vorticities are of opposite sign indicating a transfer of energy from primary to disturbance flow. At the same time, the second term of (4.1) indicates that the spatial variation of the vorticity field can interact with the velocity field to cause instability when the overall contribution is a negative quantity.

For example, for two-dimensional flows,

$$\boldsymbol{V} \cdot (\nabla \times \boldsymbol{\omega}) = u \frac{\partial \omega_z}{\partial y} - v \frac{\partial \omega_z}{\partial x}. \tag{4.2}$$

where u and v are the x- and y-components of the velocity field. In (4.2) the first term dominates in the initial stages of the instability.

If one divides E into a mean and a disturbance part, $E = E_m + \epsilon E_d$, and substitutes in (4.1), the disturbance energy equation given by (1.1) results. The corresponding linearized equation is

$$\nabla^2 E_d = 2\boldsymbol{\omega}_m \cdot \boldsymbol{\omega}_d - \boldsymbol{V}_m \cdot \nabla \times \boldsymbol{\omega}_d - \boldsymbol{V}_d \cdot \nabla \times \boldsymbol{\omega}_m, \tag{4.3}$$

which can be used to describe the onset of instability, when a suitable mean field exists. In Sengupta *et al.* (2003*b*) this method is used to explain the limiting mechanism for lift generation associated with the Magnus–Robins effect. However, here (1.1) has been used to explain the complete nonlinear evolution of disturbances.

Here the velocity and vorticity fields at $t = 20$ are taken as representative undisturbed flow. The sign of right-hand side being positive or negative indicates a sink

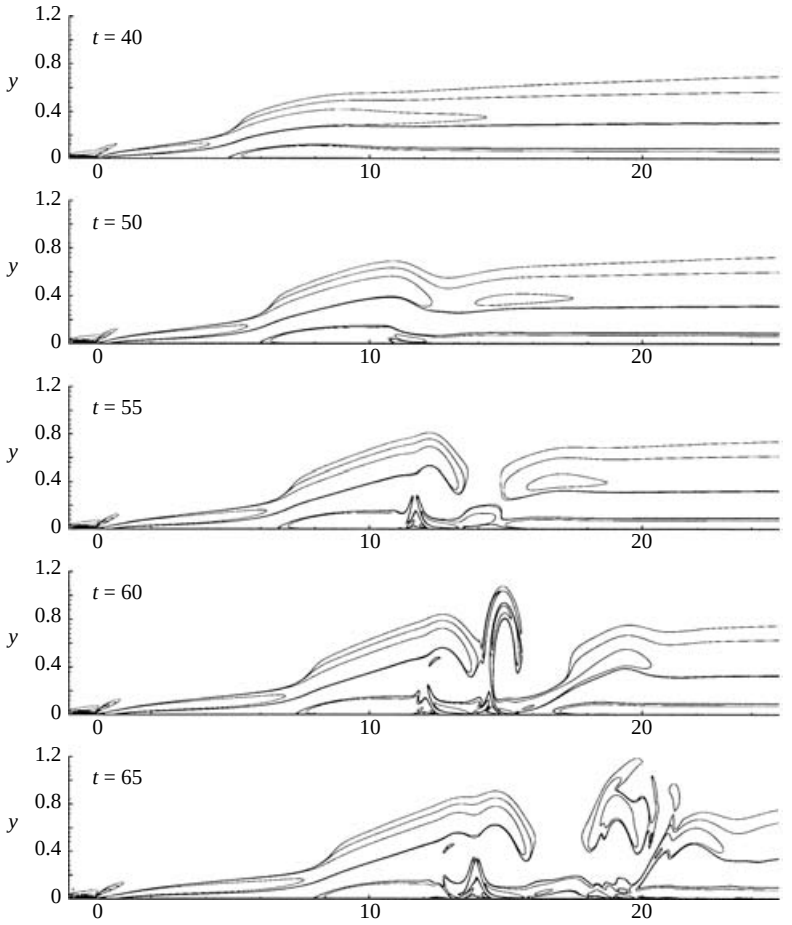

FIGURE 4. Contours of the right-hand side of the disturbance energy equation (1.1). Only the negative contours – indicating an energy source – are plotted.

or source respectively. Hence for the disturbance energy equations (1.1) or (4.3) a negative right-hand side anywhere would indicate a disturbance energy source at that point in the flow field. In figure 4, these distributed sources are plotted as negative contours, as given by (1.1). At $t = 40$, there are two sites from where instability originates – one at the leading edge and the other downstream. It is seen that the leading-edge instability is the weaker of the two and the major one originates near $x = 6$, as was also seen in figure 3. Vortical structures from these two regions interact as is evident at $t = 55$ onwards, from figures 3 and 4, where the spike forming at the downstream site is inhibited by the vortical structure originating from the leading edge.

In stream function and vorticity contour plots the spike is evident at $x = 12$ at $t = 55$ in the form of a secondary bubble. It is therefore important to include the leading edge in the analysis, otherwise one would compute the unimpeded spike stage, as in Peridier, Smith & Walker (1991) and Obabko & Cassel (2002). However, beyond $t = 55$, the instability originating from the leading edge terminates before the downstream spike and subsequently the distance between the instabilities further increases. The present analysis based on the right-hand side of (1.1) more clearly

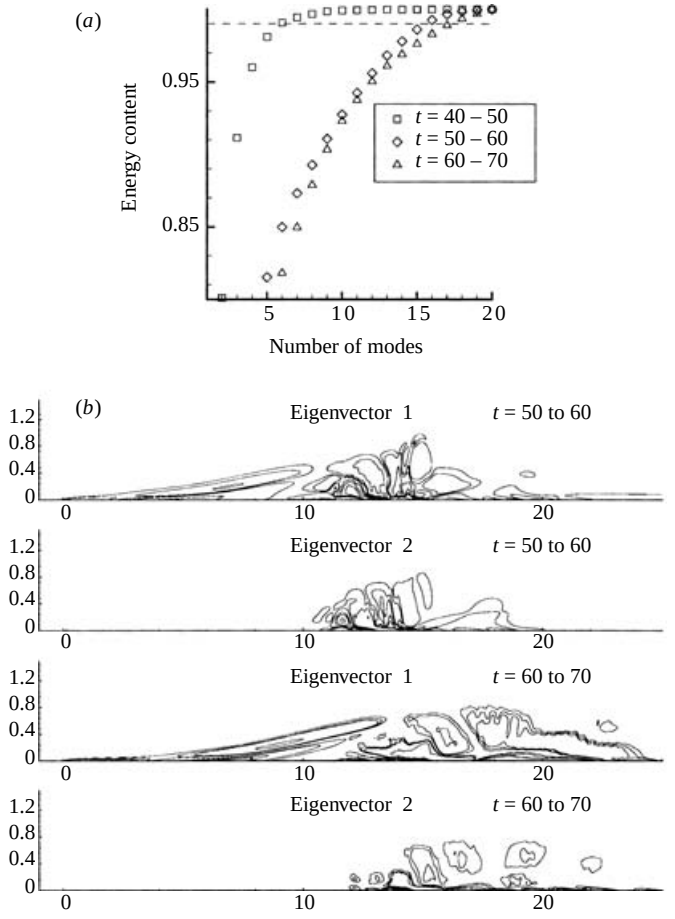

FIGURE 5. (*a*) Sum of a specific number of eigenvalues divided by total sum, indicating energy content. Dashed line marks 99% level. (*b*) The first two eigenvectors of vorticity disturbance in the indicated time ranges.

reveals the physical nature of the problem compared to the information from stream function and vorticity contours.

5. Characterizing coherent structures by POD

To visualize the coherent structures a proper orthogonal decomposition (POD) analysis is pursued next following Sirovich (1987) and Holmes, Lumley & Berkooz (1996). To hande numerical data over a large domain by POD, the *method of snapshots* by Sirovich (1987) is most appropriate, in particular if the number of input frames or snapshots is smaller than $(N_x \times N_y)$ – the product of numbers of grid points in the coordinate directions. In the present study, 21 frames have been used over time spans of 10 for performing POD. In figure 5, the eigenmodes for vorticity data over the indicated time spans are presented. The leading eigenmodes at early times clearly show two regions of sharp vorticity gradients: one starting from the leading edge $(x = 0)$ that remains invariant with time and the other emerging from downstream and representing downstream convection of large coherent structures.

This reinforces similar observations on figure 4. The terms of (4.2) contribute most where the vorticity contour lines are concentrated in space, indicating steep local gradients. The presence of a larger streamwise velocity component at the upper tier of vorticity variation would allow the instabilities to intensify more than in the lower tier by the mechanism of the terms in (4.1) and (4.2). The eigenvector 1 carries information on the instabilities experienced at the leading edge and the downstream site and the eigenvector 2, in contrast, only carries information from the downstream site. Also there is a qualitative difference in the eigenvector 1 between the first and second time interval. In the first interval the coherent structures erupt vertically, while in the later interval it shows an upstream bias. The relative importance of the eigenmodes at different time intervals can be gauged from the fraction of the total fluctuation energy contained in a specific number of leading eigenmodes and is shown in figure 5(*a*). The fractional energy content is given by the sum of the eigenvalues divided by their total sum. Up till around $t = 50$, five eigenmodes capture 99% of the total disturbance energy. This number increases to 18 during $t = 60$ to 70. It has been noted by Rajaee, Karlsson & Sirovich (1994) that this analysis method can provide insight into flow evolution at other parameter values from these eigenmodes.

Different cases have been simulated with different Reynolds numbers and strength of convecting vortex- (not shown here), which distinctly show the basic instability mechanism, though the details vary with these parameters.

6. Summary

The results of a receptivity study are reported here for an instability created on a flat-plate shear layer by a finite-core vortex convecting outside the shear layer. In the experimental study it is shown that a vortex with positive circulation creates instability ahead of it. Numerical simulation is performed for a case similar to the experiment. The coupling between the convecting vortex outside the shear layer and the generated unsteady vortical field inside is explained theoretically by developing an equation for the total mechanical energy. Finally, the unsteady vortical field created in the computation is analysed by proper orthogonal decomposition, which supports the proposed mechanism.

T. K. S. wishes to acknowledge the fellowship from Dept. of Mech. Engg., NUS (Singapore) where the experimental work was undertaken, and help of Professor T. T. Lim without whose expertise the experiments would not have been possible. The authors acknowledge various suggestions provided at different stages of this work by Professor K. R. Sreenivasan.

REFERENCES

Badr, H. M., Coutanceau, M., Dennis, S. C. R. & Menard, C. 1990 Unsteady flow past a rotating circular cylinder at Reynolds numbers 1000 and 10,000. *J. Fluid Mech.* **220**, 459–484.

Brinckman, K. W. & Walker, J. D. A. 2001 Instability in a viscous flow driven by streamwise vortices. *J. Fluid Mech.* **432**, 127–166.

Degani, A. T., Walker, J. D. A. & Smith, F. T. 1998 Unsteady separation past moving surfaces. *J. Fluid Mech.* **375**, 1–38.

Doligalski, T. L., Smith, C. R. & Walker, J. D. A 1994 Vortex interaction with walls. *Annu. Rev. Fluid Mech.* **26**, 573–616.

Haras, Z. & Ta'asan, S. 1994 Finite difference scheme for long-time integration. *J. Comput. Phys.* **114**, 265–279.

Holmes, P., Lumley, J. L. & Berkooz, G. 1996 *Turbulence, Coherent Structures, Dynamical Systems and Symmetry*. Cambridge University Press.

Landahl, M. T. & Mollo-Christensen, E. 1992 *Turbulence and Random Processes in Fluid Mechanics*. Cambridge University Press.

Monin, A. S. & Yaglom, A. M. 1971 *Statistical Fluid Mechanics: Mechanics of Turbulence*. The MIT Press.

Obabko, A. V. & Cassel, K. W. 2002 Navier-Stokes solutions of unsteady separation induced by a vortex. *J. Fluid Mech.* **465**, 99–130.

Peridier, V. J., Smith, F. T. & Walker, J. D. A. 1991 Votex-induced boundary-layer separation. Part 1. The unsteady limit problem $Re \rightarrow \infty$. *J. Fluid Mech.* **232**, 99–131.

Rajaee, M., Karlsson, S. K. F. & Sirovich, L. 1994 Low-dimensional description of free-shear-flow coherent structures and their dynamical behaviour. *J. Fluid Mech.* **258**, 1–29.

Robinson, S. K. 1991 Coherent motions in the turbulent boundary layer. *Annu. Rev. Fluid Mech.* **23**, 601–639.

Sengupta, T. K., Anuradha, G. & De, S. 2003*a* Navier–Stokes solution by new compact schemes for incompressible flow. In *Proc. 2nd MIT Conf. on Comput. Fluid and Solid Mech.* (ed. K. J. Bathe) Vol. 1, pp. 1119–1124.

Sengupta, T. K., Chattopadhyay, M., Wang, Z. Y. & Yeo, K. S. 2002 By-pass mechanism of transition to turbulence. *J. Fluids Struct.* **16**, 15–29.

Sengupta, T. K., Kasliwal, A., De, S. & Nair, M. 2003*b* Temporal flow instability for Magnus-Robins effect at high rotation rates. *J. Fluids Struct.* **17**, 941–953.

Sengupta, T. K., Lim, T. T. & Chattopadhyay, M. 2001 An experimental and theoretical investigation of a by-pass transition mechanism. *Rep. IITK/Aero/AD/2001/02*, Department of Aerospace Engineering, IIT Kanpur, India.

Sirovich, S. 1987 Turbulence and the dynamics of coherent structures. Part I : Coherent structures. *Q. Appl. Maths* **45**, 561–571.

Smith, C. R., Walker, J. D. A., Haidari, A. H. & Sobrun, U. 1991 On the dynamics of near-wall turbulence. *Phil. Trans. R. Soc. Lond.* A **336**, 131–175.

Sommerfeld, A. 1949 *Partial Differential Equation in Physics*. Academic.

Taylor, G. I. 1936 Statistical theory of turbulence. V. Effects of turbulence on boundary layer. *Proc. R. Soc. Lond.* A **156**, 307–317.